

Quantitative Precipitation Estimation from a C-Band Dual-Polarized Radar for the 8 July 2013 Flood in Toronto, Canada

SUDESH BOODOO AND DAVID HUDAK

Environment Canada, Toronto, Ontario, Canada

ALEXANDER RYZHKOV AND PENGFEI ZHANG

*Cooperative Institute for Mesoscale Meteorological Studies, University of Oklahoma,
and National Severe Storm Laboratory, Norman, Oklahoma*

NORMAN DONALDSON, DAVID SILLS, AND JANTI REID

Environment Canada, Toronto, Ontario, Canada

(Manuscript received 7 January 2015, in final form 15 May 2015)

ABSTRACT

A heavy rainfall event over a 2-h period on 8 July 2013 caused significant flash flooding in the city of Toronto and produced 126 mm of rain accumulation at a gauge located near the Toronto Pearson International Airport. This paper evaluates the quantitative precipitation estimates from the nearby King City C-band dual-polarized radar (WKR). Horizontal reflectivity Z and differential reflectivity Z_{DR} were corrected for attenuation using a modified ZPHI rain profiling algorithm, and rain rates R were calculated from $R(Z)$ and $R(Z, Z_{DR})$ algorithms. Specific differential phase K_{DP} was used to compute rain rates from three $R(K_{DP})$ algorithms, one modified to use positive and negative K_{DP} , and an $R(K_{DP}, Z_{DR})$ algorithm. Additionally, specific attenuation at horizontal polarization A was used to calculate rates from the $R(A)$ algorithm. High-temporal-resolution rain gauge data at 44 locations measured the surface rainfall every 5 min and produced total rainfall accumulations over the affected area. The nearby NEXRAD S-band dual-polarized radar at Buffalo, New York, provided rain-rate and storm accumulation estimates from $R(Z)$ and S-band dual-polarimetric algorithm. These two datasets were used as references to evaluate the C-band estimates. Significant radome attenuation at WKR overshadowed the attenuation correction techniques and resulted in poor rainfall estimates from the $R(Z)$ and $R(Z, Z_{DR})$ algorithms. Rainfall estimation from the Brandes et al. $R(K_{DP})$ and $R(A)$ algorithms were superior to the other methods, and the derived storm total accumulation gave biases of 2.1 and -6.1 mm, respectively, with correlations of 0.94. The C-band estimates from the Brandes et al. $R(K_{DP})$ and $R(A)$ algorithms were comparable to the NEXRAD S-band estimates.

1. Introduction

Traditional radar-derived rainfall estimates are based on empirical relationships between reflectivity at horizontal polarization Z and rain rate R , perhaps the most well known of these being the Marshall–Palmer power-law reflectivity and rain rate (Z – R) relation (Marshall and Palmer 1948, hereafter MP48). Reflectivity-derived rainfall estimates are known to be subjected to significant

errors (e.g., Zawadzki 1984; Austin 1987; Joss and Waldvogel 1990; Tabary 2007; Krajewski et al. 2010) and issues such as variability of the drop size distribution (DSD), attenuation, variation of the vertical profile of reflectivity (VPR), radome wetting, ground clutter, radar miscalibration, partial beam blocking, and beam filling must all be considered when deriving radar rainfall estimates. Surface rain gauges provide point measurements of rainfall and are generally considered to be the reference for radar-derived rainfall from measurements made aloft. Sampling differences in both time and space between the measurements also add to the uncertainties of radar quantitative precipitation estimation (QPE; e.g., Zawadzki 1975, 1984).

Corresponding author address: Sudesh Boodoo, Cloud Physics and Severe Weather Research Section, Environment Canada, 14780 Jane St., King City, ON L7B 1A3, Canada.
E-mail: sudesh.boodoo@ec.gc.ca

Dual-polarization radar technology provides additional information about atmospheric targets from the transmission and reception of horizontally H and vertically V polarized waves. Complementing horizontal reflectivity, differential reflectivity Z_{DR} , differential propagation phase Φ_{DP} , specific differential phase K_{DP} , and the copolar correlation coefficient ρ_{HV} provide additional information to help mitigate some of the issues with QPE derived from single-polarization radars. Numerous dual-polarimetric rain-rate estimators at S, C, and X bands have been described in the literature (e.g., Scaichilli et al. 1993; Bolen et al. 1998; Bringi and Chandrasekar 2001, hereafter BR01; Gorgucci et al. 2001; Ryzhkov et al. 2005a,b; Illingworth and Thompson 2005; Tabary et al. 2011). Such rain-rate estimators are generally of the forms $R(Z)$, $R(Z, Z_{DR})$, $R(K_{DP})$, and $R(K_{DP}, Z_{DR})$, where Z and Z_{DR} are corrected for attenuation using dual-polarimetric measurements. Dual-polarimetric measurements can be used to discriminate between meteorological and nonmeteorological echoes (BR01). Removal of nonmeteorological targets (e.g., Ryzhkov and Zrnić 1998a; Liu and Chandrasekar 2000; Gourley et al. 2007) directly aids QPE, and the separation of the meteorological targets into hydrometeor classes means appropriate rainfall estimators can be applied (Giangrande and Ryzhkov 2008; Park et al. 2009; Cifelli et al. 2011). Recently, Ryzhkov et al. (2014, hereafter R14) have developed a rainfall estimation algorithm using horizontal specific attenuation A , which mitigates problems with radar miscalibration, partial beam blockage, DSD variability, and wet radome, which are problematic for estimators relying on Z and Z_{DR} and less so for K_{DP} estimators. The studies by Ryzhkov et al. (2014), Giangrande et al. (2014), Wang et al. (2014), and Diederich et al. (2015a,b) demonstrate good performance of the $R(A)$ estimators at S, C, and X bands in different parts of the world.

On 8 July 2013, a series of thunderstorms developed over the city of Toronto, Canada, producing heavy rainfall and flash flooding and making an excellent case study for radar QPE methods at C band. Gauges distributed across the city recorded 5-min precipitation amounts during the event, and a few more recorded total accumulation only. The Next Generation Weather Radar (NEXRAD) S-band dual-polarimetric radar at Buffalo, New York (KBUF; ~ 100 km south of Toronto), had a clear view of the storms over Toronto, and the dual-polarimetric data collected from that radar provided additional estimates of the precipitation over the city. The objective of this study is to assess the quantitative precipitation estimation of rainfall for the C-band radar and to demonstrate the dual-polarization potential for precipitation estimation in extreme weather. The

paper is organized as follows. A synoptic description of the event is presented in section 2. Section 3 describes the gauge and the NEXRAD S-band radar datasets, followed by details of the C-band radar data processing and QPE algorithms. Results for the radar-derived estimates and comparisons with the gauges are presented in section 4, followed by the conclusions in section 5.

2. Event description: Meteorological analysis

On 8 July 2013, a weak low pressure system supported by an upper-level trough advected a warm and humid air mass over much of southern Ontario, allowing for the development of several areas of short-lived, slow-moving, “pulse”-type thunderstorms. There were no damaging winds or hail with these storms, but very heavy rain fell across portions of southern Ontario, causing localized but significant flash flooding.

During the morning, the weather system, initially over eastern Wisconsin, tracked eastward toward Lake Huron. By midafternoon, there was an associated weak east-to-west stationary front/surface pressure trough approximately 150 km north of Toronto. Temperatures south of the front were in the mid to high 20°C range, with dewpoints of 20°–22°C. Figure 1 shows the Buffalo sounding at 0000 UTC 9 July. Aside from a low-level inversion due to flow off Lake Erie, the sounding was representative of the conditions in the Toronto area. It indicated weak winds aloft (<15 m s⁻¹), weak shear at 0–6 km (<9 m s⁻¹), and high precipitable water (near 40 mm).

Around 1700 UTC [1300 local time (LT)], a small cluster of thunderstorms developed about 100 km north of Toronto. Storms moved slowly to the southeast (<5 m s⁻¹). By 2015 UTC (1615 LT), the thunderstorms had reached the northern part of Toronto, now moving southward at about 6 m s⁻¹ after encountering the north–south–oriented Lake Ontario lake-breeze front. An outflow boundary generated by the thunderstorms converged with the lake-breeze front, leading to convective development and an expanded area of moderate-to-heavy rain farther south and westward at 2030 UTC (1630 LT). This affected the Toronto Pearson International Airport (CYYZ) area and most of the western half of the city.

At 2100 UTC, the storm continued to track slowly southward following the intersection point of the outflow boundary (black) and the lake-breeze front (magenta), shown in Fig. 2 [mesoscale boundary identification methods described in Sills et al. (2011)]. The heavier rainfall ended west of CYYZ while the core of the heavy rain was located in the area from the CYYZ area eastward to central parts of Toronto. By this time,

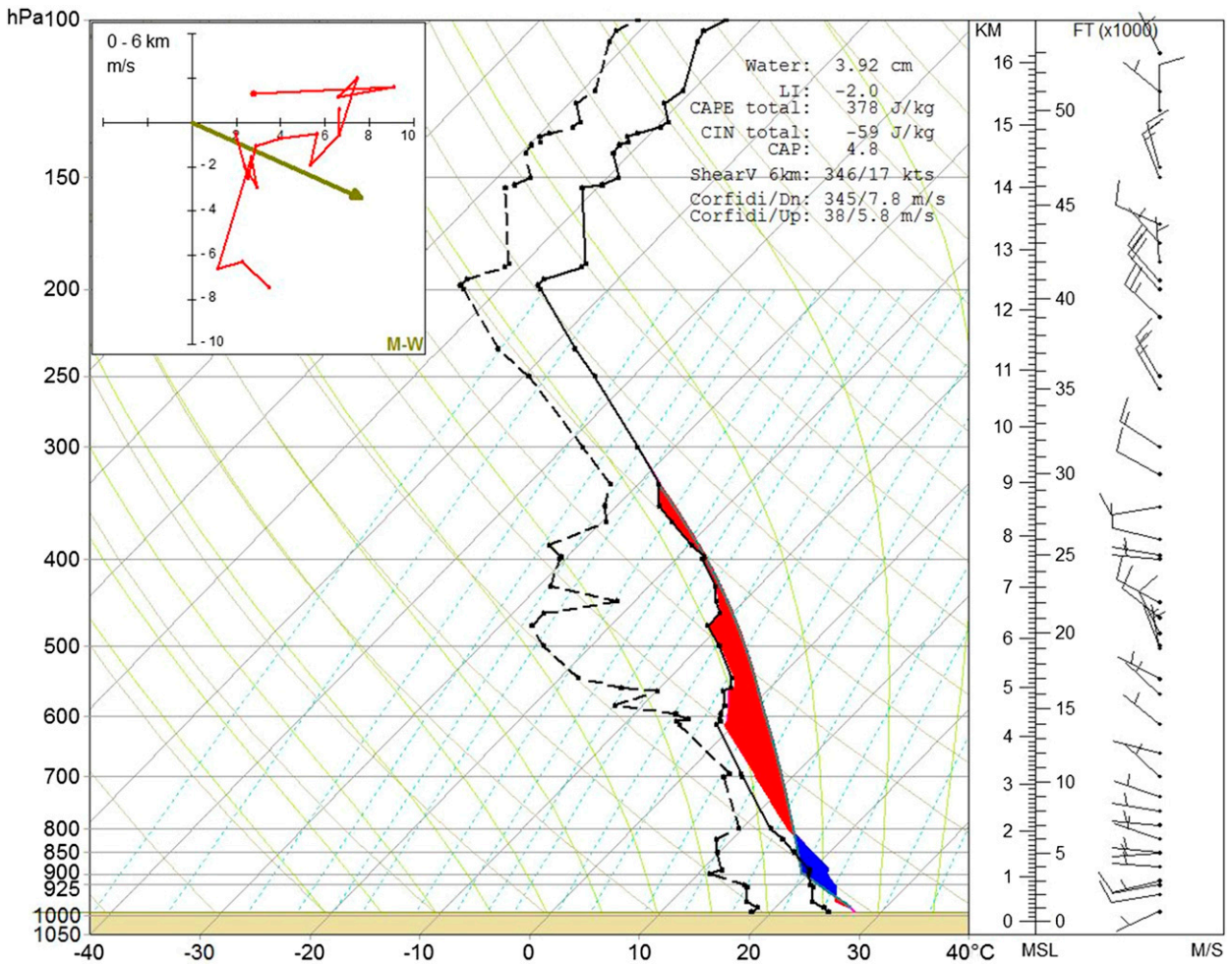


FIG. 1. KBUF balloon sounding at 0000 UTC 9 Jul 2013 with temperature (solid black curve), dewpoint (dashed black curve), positive CAPE (red area), and convective inhibition (CIN; blue area). CAPE is calculated using the virtual temperature correction and the most unstable parcel in the lowest 300 hPa. The hodograph is shown in red at top left, with the mean wind in the cloud-bearing layer shown by the gold arrow (m s^{-1}). The wind profile is shown at right (short barb = 5 m s^{-1} ; long barb = 10 m s^{-1}).

another weaker line of thunderstorms had formed north and west of Toronto along the outflow boundary from earlier storms. This second line reached CYYZ at 2120 UTC (1720 LT). Storms along this second line, unaffected by the lake-breeze front, took on a more southeastward movement and concentrated the precipitation in the area already affected by heavy rain (from CYYZ to downtown Toronto) over the next 2 h. The combined effects of slow-moving storms and high precipitable water values, enhancement due to boundary interactions, and the same area being affected twice led to the local extreme values of precipitation. The further combination of this extreme rainfall with the urban landscape resulted in significant flash flooding.

The majority of rain fell from approximately 2020 to 2230 UTC (1620 to 1830 LT), a duration of approximately 2 h. CYYZ received a total of 126.0 mm of rain,

surpassing the 1-day record of 121.4 mm set in 1954 (the so-called Hurricane Hazel event).

3. Data description

a. Rain gauge

Surface rainfall amounts were provided from 48 gauges, of which 44 were tipping-bucket rain gauges (TBRG) operated and maintained by the Toronto and Region Conservation Authority (TRCA) and the City of Mississauga. Rainfall amounts in time increments of 5 min were available from the 44 TBRG gauges. The remaining four gauges were operated by Environment Canada (EC) and provided only the storm total accumulation. The gauges were distributed around the region of the heaviest rainfall for the event and all were

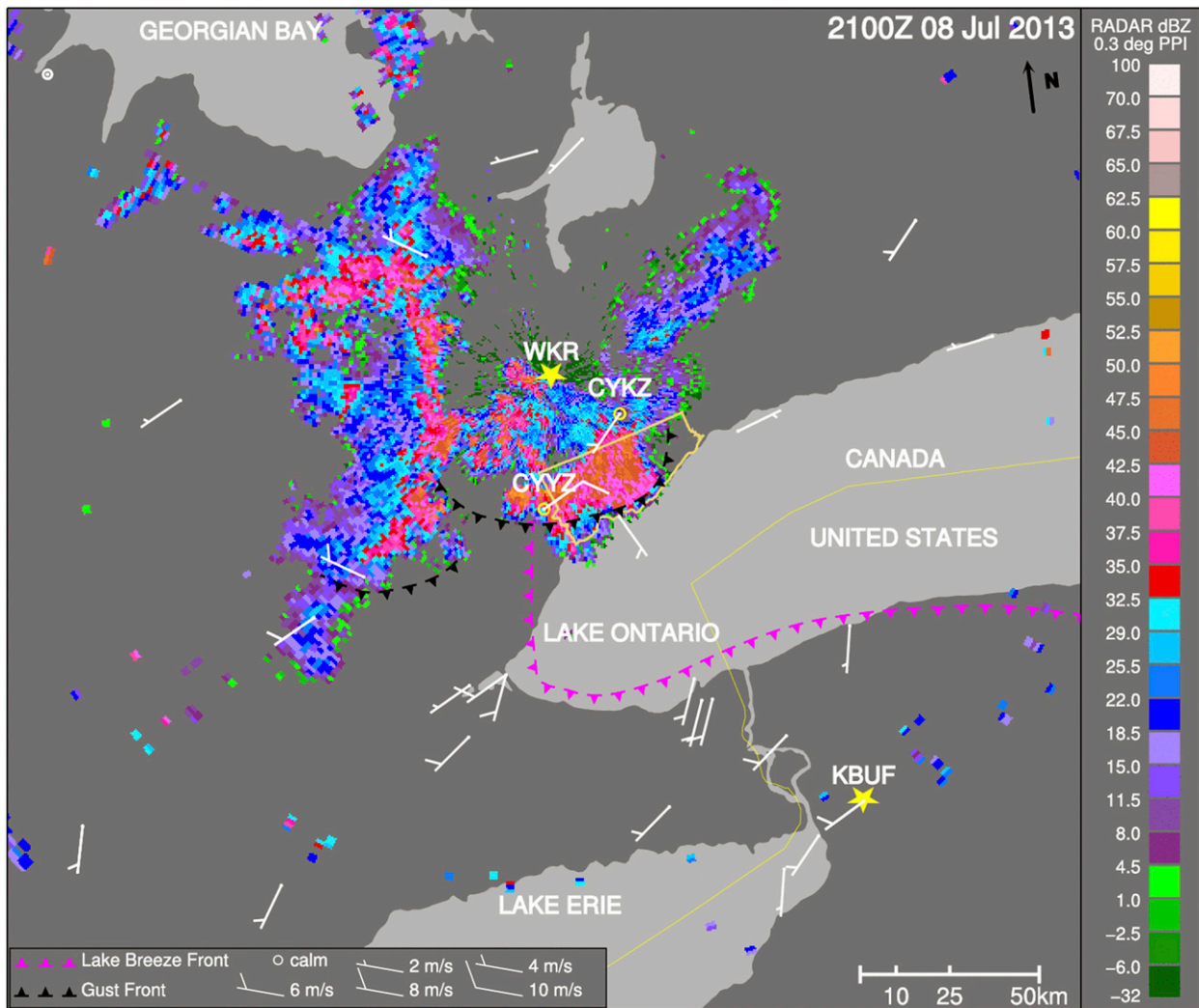


FIG. 2. Mesoscale wind analysis with radar echoes overlaid at 2100 UTC 8 Jul 2013. The lake-breeze front is indicated by the magenta line and the storm outflow is shown in black. Yellow stars indicate WKR and KBUF. Surface winds at CYYZ and Buttonville Municipal Airport (CYKZ) are shown with magnitudes indicated by the barbs.

within 55 km of the radar. The maximum gauge rainfall total for the storm was 126.0 mm, for the EC gauge located at CYYZ. King City C-band dual-polarized radar (WKR; Fig. 2) is located 32 km north of CYYZ. Figure 3 shows the rain gauge locations and storm total accumulations for the event over the greater Toronto area.

b. S-band radar

The Weather Surveillance Radar-1988 Doppler (WSR-88D) network began an upgrade in 2011 to the NEXRAD to dual-polarization technology across the United States. Dual-polarimetric rain-rate algorithms such as $R(Z, Z_{DR})$, $R(Z, K_{DP})$, and $R(K_{DP})$ were developed by Ryzhkov et al. (2005b) and were shown to outperform standard single-polarimetric $R(Z)$ algorithms. Additionally, rainfall estimates contingent on

hydrometeor classification, for example, Giangrande and Ryzhkov (2008) and Park et al. (2009), are used for QPE in the WSR-88D system. The processing chain for these dual-polarimetric QPEs (DP-QPEs) for WSR-88D can be found in Berkowitz et al. (2013). Recent assessment of the NEXRAD DP-QPE algorithms has been studied by Cocks et al. (2012) and Cunha et al. (2013). Their assessment was performed over various spatial and temporal scales and under various precipitation conditions. In general, the DP-QPE algorithms performed better than the traditional Z -based methods. A new $R(A)$ algorithm to be implemented for NEXRAD shows very promising results (Ryzhkov et al. 2014).

The Buffalo, New York, NEXRAD S-band radar is located 106 km south-southeast of CYYZ and 156 km from WKR (Fig. 2). During the event the radar was

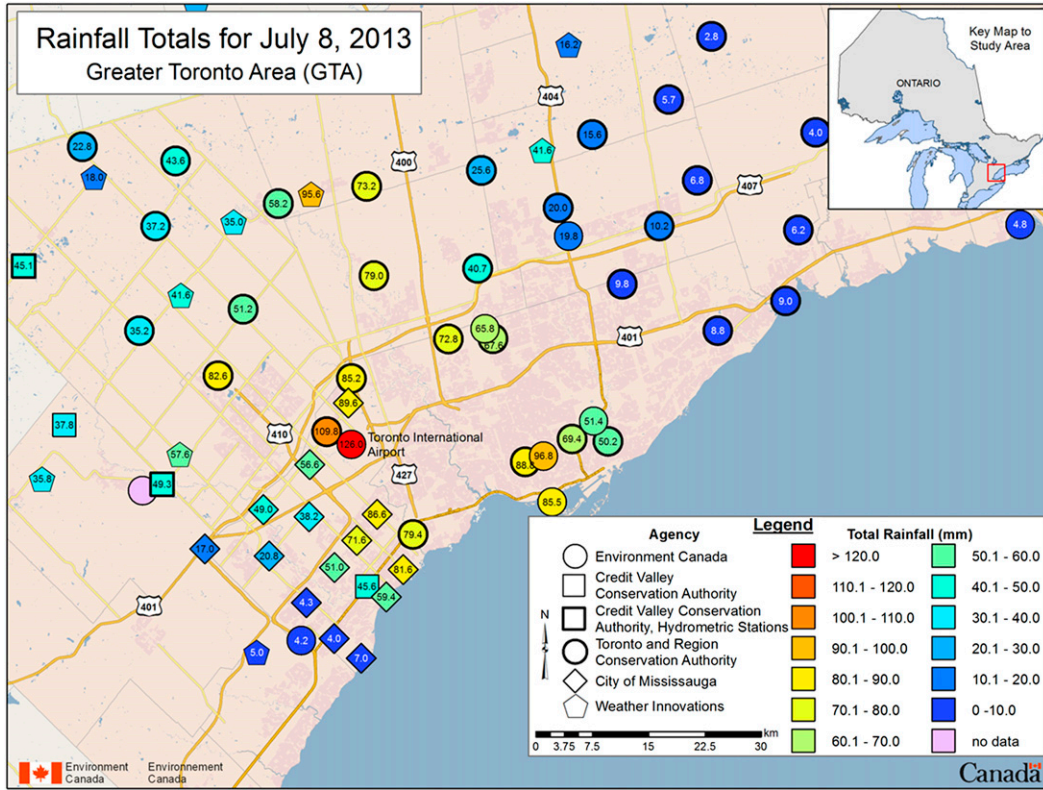


FIG. 3. Storm total rainfall accumulations at gauges from different organizations distributed around the greater Toronto area. Various symbols indicate the operating authority responsible for the gauges. The EC gauges (thin circles) reported only total storm accumulation. The others were TBRGs measuring in 5-min intervals.

scanning in precipitation mode and collected dual-polarimetric data about every 6 min at spacings of 0.25 km in range and 0.5° in azimuth. KBUF level-II Z , Z_{DR} , ρ_{HV} , and Φ_{DP} from the 0.5° elevation were used for the analysis and compared with the WKR 0.5° elevation scans at matching times. The WSR-88D estimates of rainfall using the $R(Z)$ and DP-QPE algorithms were generated over the Toronto area for comparison with rain gauges and C-band rainfall retrievals.

c. C-band radar

WKR operates in simultaneous transmit–receive horizontal–vertical mode, and signal processing is done with a Sigmet RVP900 processor. Several scanning tasks are performed, one of which collects the dual-polarimetric data, collecting 64 samples with dual PRF of 1000/750 Hz at 0.5° elevation polarimetric plan position indicator (POLPPI). The task is completed in 1 min with 0.25 km × 0.5° range and azimuthal resolution. Its maximum range is 150 km. Additional scans are performed that make up a 10-min data collection cycle. Ground clutter returns from buildings, trees, etc. are removed at the signal processor level using a fixed-width clutter filter (removal of the zero velocity bin and two points on either side). Subsequently,

thresholding by signal quality index ($SQI > 0.05$), signal-to-noise ratio ($LOG > 2$ dB), and clutter-to-signal ratio ($CSR > 25$ dB) are applied to reflectivity and the dual-polarimetric data. Such filtering and thresholding turns out to be efficient in removing most of the clutter in the urban environment.

d. C-band postprocessing

Reflectivity and differential reflectivity were corrected for attenuation using a modified form of the traditional ZPHI rain profiling algorithm by Testud et al. (2000). In their algorithm, the change in Z and Z_{DR} for attenuation were estimated from

$$\Delta Z = \alpha \Phi_{DP} \quad \text{and} \quad \Delta Z_{DR} = \beta \Phi_{DP}, \quad (1)$$

where α is the ratio of the horizontal specific attenuation A to K_{DP} and β is the ratio of specific differential attenuation A_{DP} to K_{DP} . Profiles of Φ_{DP} were unfolded, if necessary, and smoothed to remove nonmeteorological signals by using a 3.0-km window within the range of intervals where $\rho_{HV} > 0.85$, and then they were linearly interpolated between these intervals (Ryzhkov et al. 2005a). The traditional method assumes α and β are

constant; however, they are affected by uncertainties in temperature and raindrop shape and are also sensitive to resonance scattering effects at C band (Ryzhkov et al. 2006). A modified ZPHI attenuation correction for Z and Z_{DR} for C band by Ryzhkov et al. (2006, 2007) and Gu et al. (2011) that relies on identification of hotspots (contiguous regions in rain cells that contain large drops and possibly hail) along the radials was implemented. Initial attenuation correction of Z and Z_{DR} were applied according to Eq. (1). The hotspot cell was identified if the corrected reflectivity exceeded 45 dBZ and ρ_{HV} was greater than 0.85 and extended for at least 2.0 km for consecutive range bins. Alternatively, hotspots could be identified from Z_{DR} where regions along the ray were greater than 3 dB, $25 < Z < 45.0$ dBZ, and $\rho_{HV} > 0.85$. The α and β parameters in Eq. (1) are highly variable inside hotspots, and assuming them to be constants is no longer valid. Inside the hotspot regions, α is a variable with range r , $\alpha(r) = \alpha_0 + \Delta\alpha(r)$, with $\alpha_0 = 0.06 \text{ dB deg}^{-1}$ as a constant value (Ryzhkov et al. 2005a, 2006, 2007). The parameter $\Delta\alpha$ is determined by an iterative process that satisfies

$$\int_{Z < Z_t} A(r, \Delta\alpha) dr = \frac{\alpha_0}{2} \Delta\Phi_{DP}(Z < Z_t = 45 \text{ dBZ}) \quad (2)$$

and

$$\Delta\Phi_{DP}(Z < Z_t) = \Delta\Phi_{DP}(r_0; r_m) - \Delta\Phi_{DP}(Z > Z_t = 45 \text{ dBZ}). \quad (3)$$

Here, Z_t is the intrinsic reflectivity threshold (45 dBZ) and $r_0; r_m$ is the range interval for which the total span of Φ_{DP} satisfies the ρ_{HV} criteria above; and dr is the incremental range. Correction for differential reflectivity is performed in a similar manner to reflectivity attenuation correction. Outside hotspot regions, β in Eq. (1) is assumed constant, $\beta = 0.017 \text{ dB deg}^{-1}$. Inside hotspots, $\beta = \beta_0 + \Delta\beta$, and the bias of Z_{DR} along the beam on the far side of the attenuation interval is determined as

$$\Delta Z_{DR}(r) = \beta_0 \Phi_{DP}(r) + \Delta\beta \Delta\Phi_{DP} \quad (4)$$

and

$$\Delta\beta = \{Z_{DR} - \min[Z_{DR}(r, \beta_0)]\} / \Delta\Phi_{DP}. \quad (5)$$

Ryzhkov et al. (2007) investigated convective storms in southern Ontario from the King City radar to derive estimates of rain rates from the correction of Z and Z_{DR} with the hotspot identification method. Using the above constant values for α_0 and β_0 in the hotspot correction techniques agreed better with $R(K_{DP})$ rainfall estimates than rate estimates from the traditional ZPHI method (Ryzhkov et al. 2007). The dual-polarimetric measurements

were contaminated with second-trip returns. Radar pixels with SQI lower than 0.4 and ρ_{HV} smaller than 0.85 were removed, resulting in the elimination of most of the spurious second-trip signatures. In areas of precipitation, the radar returns overwhelmed any second-trip contamination.

Specific differential phase was calculated from the Φ_{DP} profiles after dealiasing and removal of range gates with ρ_{HV} less than 0.9. This profile was smoothed over 6.0 km and interpolated to fill gaps that resulted from the ρ_{HV} threshold. From the processed Φ_{DP} profile, K_{DP} was derived by using a least absolute deviation fit over six range bins or 1.5 km.

Scans at 0.5° elevation are shown in Fig. 4 of uncorrected Z and Z_{DR} , measured Φ_{DP} , and ρ_{HV} from WKR at 2030 UTC 8 July 2013. CYYZ is located at the intersection of the red lines at the center of the figures. The first wave of heavy rainfall had just passed over the radar and was now over the airport area. At the airport for this time Z was in the 35–40-dBZ range, and 40–45 dBZ in the more intense parts of the storm to the northeast. Overall Z_{DR} was high, with values over 3 dB in pockets to the northeast of CYYZ. In the high-reflectivity areas (40–45 dBZ), Z_{DR} was in the 1–2-dB range. The large area of negative (from -0.5 to -4 dB) Z_{DR} in Fig. 4b, at the southern edges of the storm, shows the most attenuated areas, a combination of a wet radome and path attenuation. The Φ_{DP} gradients are also very large in these negative Z_{DR} areas (Fig. 4c). The initial Φ_{DP} close to the radar was about 20° , and then rapidly increases to over 220° over a distance of about 20 km. The ρ_{HV} for the most part (Fig. 4d) was greater than 0.98 even in attenuated areas; however, there were small pockets of lower ρ_{HV} (0.95) corresponding to large gradients in Φ_{DP} . In addition, resonance scattering effects by large drops could also reduce ρ_{HV} in these cores.

Figures 5a and 5b show the reflectivity and differential reflectivity from WKR corrected for attenuation as outlined in Eqs. (1)–(5). Corrected Z in Fig. 5a at the airport has increased by about 5 dBZ compared to the uncorrected value (Fig. 4a). The overall reflectivity pattern has increased by about the same amount, and the stronger cores were now mostly in the 45–50-dBZ range, even up to 55 dBZ in some small localized areas. Figure 5c shows the reflectivity obtained from KBUF. Reflectivity from KBUF at CYYZ was in the 50–55-dBZ range, and greater than 60 dBZ can be seen in rain cells farther to the northeast of the airport. The C-band attenuation correction scheme is undercorrecting Z by 5–10 dB overall, and up to 15 dB in certain areas. Several factors can account for this large overall undercorrection of Z . The heavy rain cell had just passed over the radome and inappropriate α in the primary attenuation correction for Z resulted in large areas being undercorrected. This would also compromise hotspot identification along certain radials, resulting in low overall

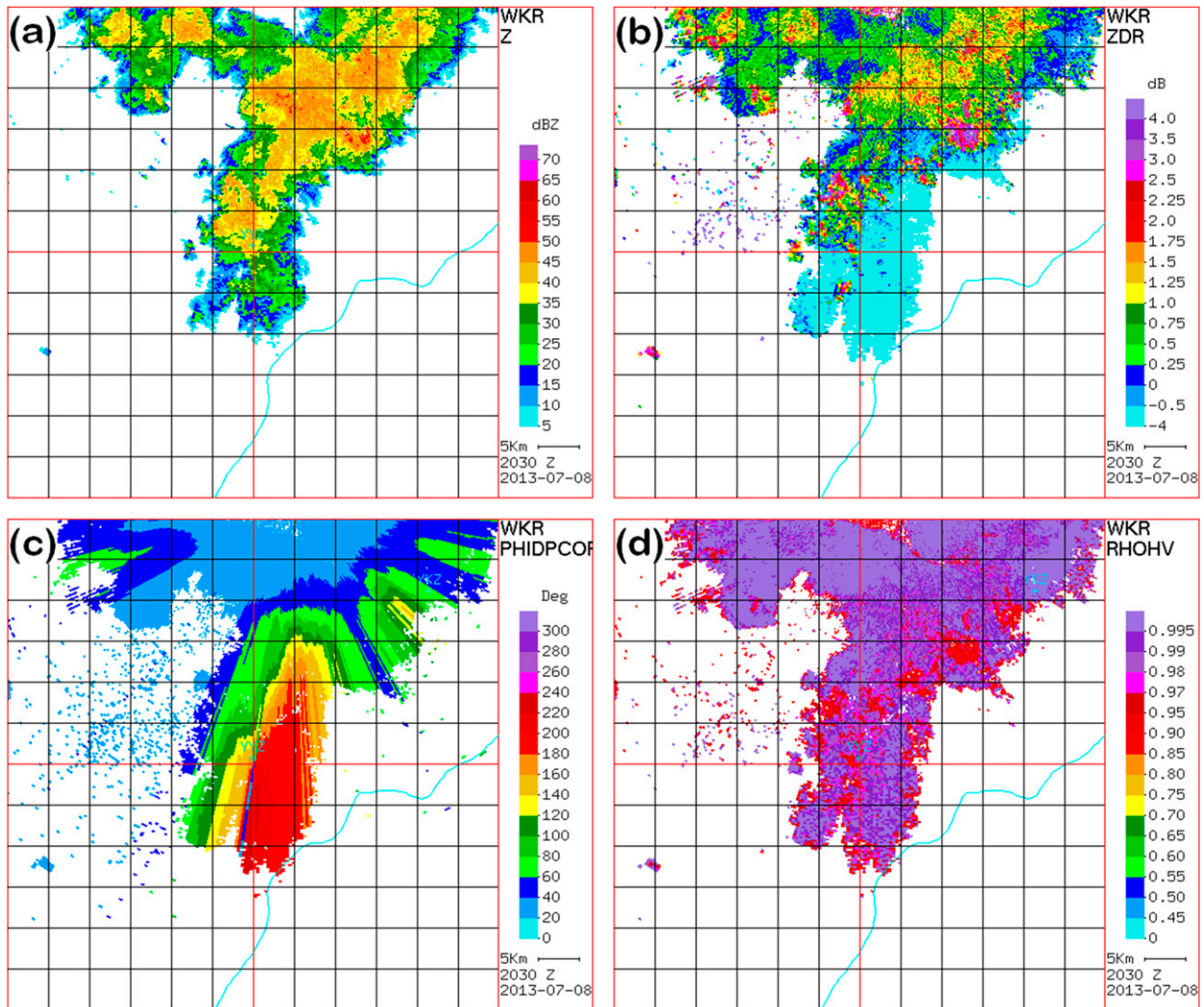


FIG. 4. WKR 0.5° elevation scans of (a) Z , (b) Z_{DR} , (c) Φ_{DP} , and (d) ρ_{HV} at 2030 UTC 8 Jul 2013. CYYZ is at the center of the image.

Z bias. The C-band-corrected Z_{DR} and S-band Z_{DR} are shown in Figs. 5b and 5d, respectively. The far side of the cell that originally had large areas of negative Z_{DR} has now been corrected and compares well with the S-band Z_{DR} patterns. The 60-dBZ reflectivity cores from KBUF show Z_{DR} in the 2.5–3.5-dB range, and the C-band attenuation-corrected Z_{DR} gave similar values. For a few areas on the far side of the echoes where the Z_{DR} correction fails, Z_{DR} remains negative. The β value initially applied along these azimuthal directions may not have been sufficient to allow hotspot identification and resulted in undercorrection of Z_{DR} at these ranges. The S-band pixels of Z_{DR} in the corresponding poorly corrected areas range from about 0.25 to 1.0 dB. Note also that the corrected Z_{DR} in Fig. 5b shows a few spurious radials in the directions of the two large S-band Z_{DR} cores in Fig. 5d and can be fixed by considering azimuthal continuity (Gu et al. 2011).

At certain times, heavy rain over the radome and its associated losses upon transmission and reception were even more problematic for this 8 July case compared to times with just a wet radome. Figures 6a–c show uncorrected Z (Fig. 6a), corrected Z (Fig. 6b), and corrected Z_{DR} (Fig. 6c) at 2100 UTC, a time with little or no rain at WKR. There is an overall change of a few decibels from uncorrected Z to corrected Z and also pockets of large corrected Z_{DR} (3–4 dB) just north of the airport. Soon afterward, a heavy band of precipitation moved over the radar and persisted, causing significant radome attenuation. Figures 6d–f show WKR uncorrected Z (Fig. 6d), corrected Z (Fig. 6e), and corrected Z_{DR} (Fig. 6f) at 2200 UTC, while it was still raining heavily at the dome. Overall, the attenuation correction increased Z in parts of the storm by about 10 dB, and negative Z_{DR} has been increased to 2–3 dB after correction (Fig. 6f).

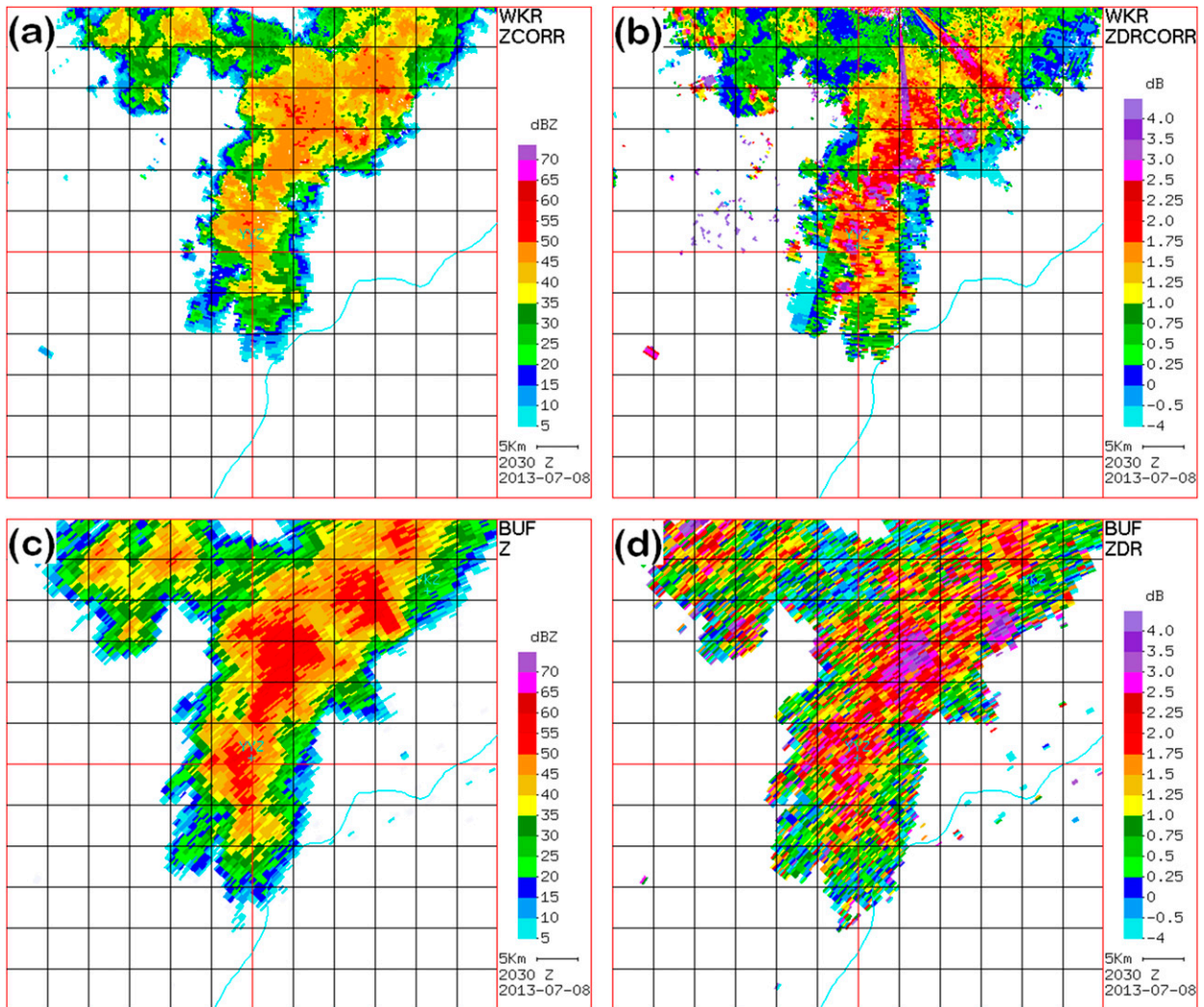


FIG. 5. WKR 0.5° elevation scans of (a) corrected Z and (b) corrected Z_{DR} and KBUF 0.5° elevation scans of (c) Z and (d) Z_{DR} at 2030 UTC 8 Jul 2013.

Figures 6g–i are the KBUF scans of Z (Fig. 6g), Φ_{DP} (Fig. 6h), and Z_{DR} (Fig. 6i) at 2200 UTC. In the strongest areas of the storm (~ 15 km south of CYYZ), the S-band reflectivity is about 15–20 dB higher overall than the uncorrected C-band reflectivities and 10–15 dB higher than the C-band-corrected reflectivities. Even for KBUF there are regions of large radial Φ_{DP} changes (from 20° to over 200°), as seen in Fig. 6h, suggesting that even the signal at S band suffers from attenuation. The large Φ_{DP} gradients correspond to areas of negative Z_{DR} (Fig. 6i) and a reduced reflectivity pattern at the far end of the rain cell (Fig. 6g).

e. QPE

Rainfall estimates were determined from Z , Z_{DR} , K_{DP} , and A for each of the POLPPI scans at 10-min

intervals. Table 1 lists the rain-rate estimators that were used. Since there was significant attenuation throughout most of the storm, all the rate estimates based on Z and Z_{DR} also utilized the attenuation-corrected values. Note that the Z – R relationship from Richards and Crozier (1983) for the King City radar is very similar to the U.S.-derived relationship (Fulton et al. 1998, hereafter F98). As such, only the latter was used for evaluation of the rainfall amounts. The multiparameter rain-rate estimators $R(Z, Z_{DR})$ and $R(K_{DP}, Z_{DR})$ from BR01, with appropriate coefficients for C band, were used to derive the rain rates. Several $R(K_{DP})$ algorithms were tested with varying coefficients determined at a variety of geographical locations. The Brandes et al. (2002, hereafter B02) algorithm was developed in Florida using a dense rain gauge network and disdrometer observations.

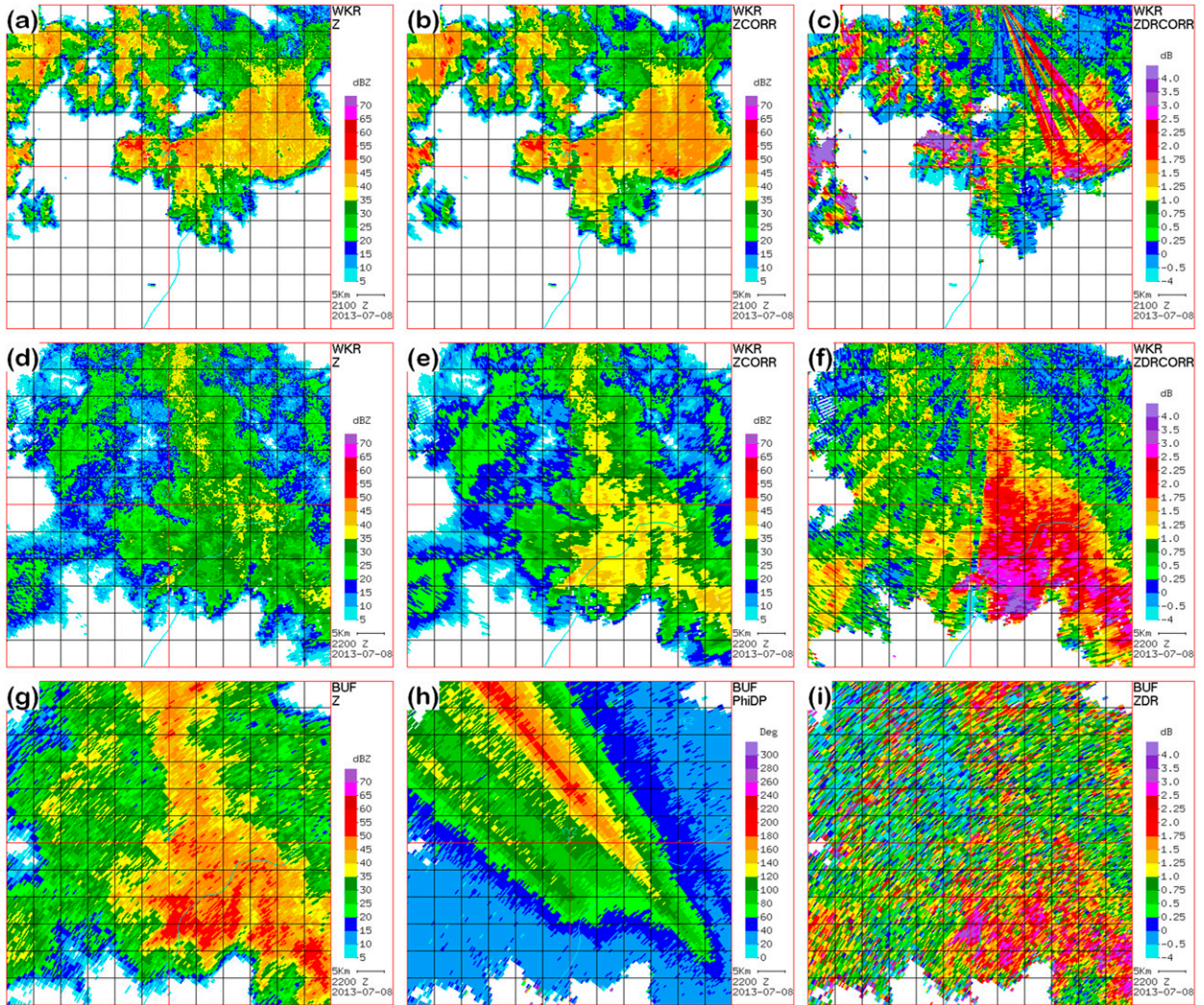


FIG. 6. WKR 0.5° elevation scans of (a) Z , (b) corrected Z , (c) corrected Z_{DR} at 2100 UTC 8 Jul 2013. (d)–(f) As in (a)–(c), but for 2200 UTC. KBUF 0.5° elevation scans of (g) Z , (h) Φ_{DP} , and (i) Z_{DR} at 2200 UTC.

The [Bringi et al. \(2006, hereafter BR06\)](#) $R(K_{DP})$ relationship was derived from 2D video disdrometer (2DVD) data for a subtropical event with a heavy convective cell embedded in stratiform rain in Japan. The [Bringi et al. \(2011, hereafter BR11\)](#) $R(K_{DP})$ relation was developed for C band in the United Kingdom, using Joss disdrometer data during the convective season. The derived K_{DP} in our processing produced negative K_{DP} pixels in areas of lighter rain during the event and are considered to be associated with strong reflectivity gradients at the rear of the storm cells ([Ryzhkov and Znić 1996, 1998b](#)). Since negative K_{DP} would imply negative rain rates, three $R(K_{DP})$ estimators were evaluated using only positive K_{DP} pixels. As pointed out by several studies evaluating rainfall using positive- and positive–negative specific differential phase

(e.g., [Brandes et al. 2001; Cifelli et al. 2011](#)), the use of positive-only K_{DP} tends to overestimate rainfall. A modified B02 algorithm similar to that suggested by [Ryzhkov and Znić \(1998b\)](#) and listed in [Table 1](#) was used to evaluate rainfall accumulation using both negative and positive K_{DP} to become the fourth $R(K_{DP})$ (hereafter called B02*) estimator for the event.

The $R(A)$ relation from R14 with the factor $\alpha = 0.08 \text{ dB deg}^{-1}$, optimized for 20°C, was utilized in our analysis. Rainfall estimation from the KBUF WSR-88D was done with the standard “thunderstorm” $R(Z)$ relation (F98),

$$R(Z) = 1.7010^{-2} Z^{0.714}, \quad (6)$$

TABLE 1. List of rain-rate estimators from various algorithms based on combinations of Z , Z_{DR} , and K_{DP} .

Reference	Origin	Formula
MP48	Canada	$R = 0.0365Z^{0.625}$
F98	United States	$R = 0.017Z^{0.714}$
BR01		$R = 0.0058Z^{0.91}10^{-0.209Z_{DR}}$
BR01		$R = 37.9K_{DP}^{0.89}10^{-0.072Z_{DR}}$
R14		$R = 294A^{0.89}$ ($T = 20^{\circ}\text{C}$)
BR11	United Kingdom	$R = 25K_{DP}^{0.81}$
BR06	Japan	$R = 29K_{DP}^{0.85}$
B02	Florida	$R = 33.8K_{DP}^{0.79}$
B02*	Florida	$R = \text{sign}(K_{DP})33.8 K_{DP} ^{0.79}$

and the polarimetric algorithm (DP-QPE), which prescribes the use of the $R(Z, Z_{DR})$ relation

$$R(Z, Z_{DR}) = 6.7010^{-3} Z^{0.927} Z_{DR}^{-3.43} \quad (7)$$

in pure rain (not contaminated by hail, snow, and mixed-phase hydrometeors). The Z and Z_{DR} in Eqs. (6) and (7) are expressed in linear scale.

4. Results

From the list of rain-rate relationships listed in Table 1, it was possible to derive 13 C-band estimates of total rainfall in all for the C-band data. They consisted of various combinations of uncorrected and corrected Z and Z_{DR} for the $R(Z)$ and $R(Z, Z_{DR})$ algorithms. Similarly, combinations of uncorrected and corrected Z_{DR} and K_{DP} were derived from the $R(K_{DP}, Z_{DR})$ algorithms and then the purely $R(K_{DP})$ algorithms. The thirteenth C-band estimate was from the $R(A)$ method. Including the two storm total estimates from the Buffalo S-band radar, the total number of rainfall estimates was 15 for the event.

a. Intercomparison of spatial accumulation patterns

Figure 7 presents 10 of the 14 radar-derived estimates for total event rainfall: eight are from the C-band radar and two are from the S-band radar. Those not shown are the four C-band storm accumulations based on the algorithms that used the uncorrected Z and Z_{DR} . Figures 7a and 7b show the rainfall total based on the MP48 and F98 algorithms for WKR using the attenuation-corrected reflectivities. Figures 7c and 7d are for the $R(Z, Z_{DR})$ and $R(K_{DP}, Z_{DR})$ algorithms using the attenuation-corrected Z and Z_{DR} . Figures 7e–g are accumulations from the BR11, BR06, and B02 $R(K_{DP})$ algorithms, respectively. Figure 7h is for the R14 $R(A)$ algorithm, and Figs. 7i and 7j are the S-band-derived storm accumulations from $R(Z)$ and $R(Z, Z_{DR})$ relations [Eqs. (6) and (7)].

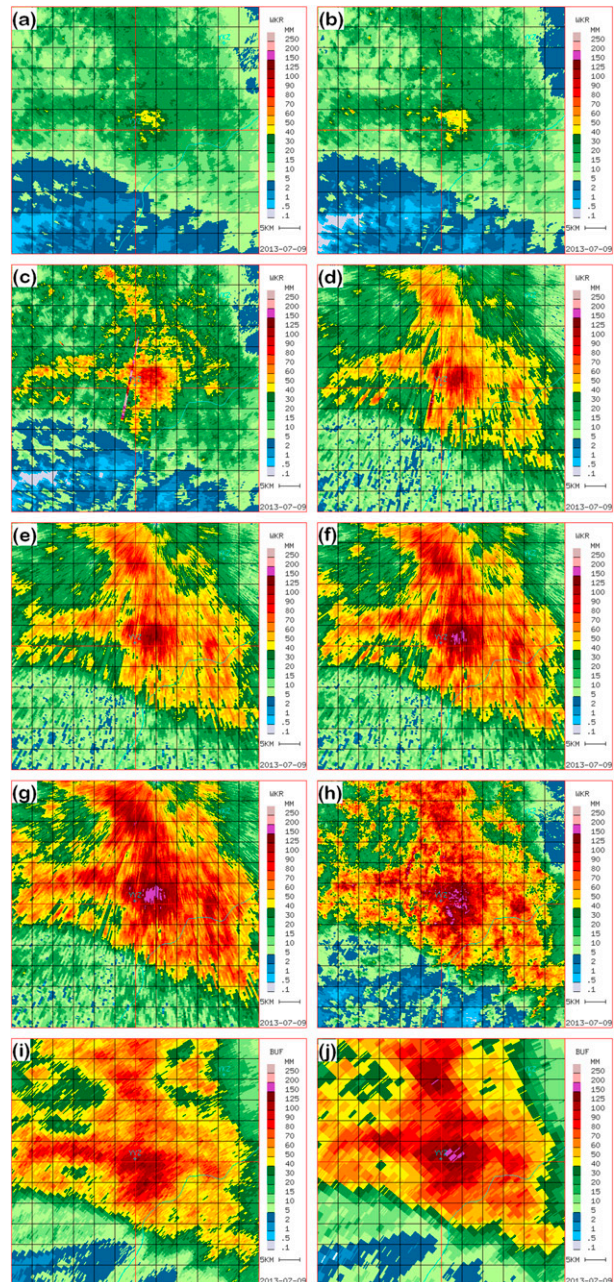


FIG. 7. Storm total accumulations using the attenuation-corrected reflectivity and differential reflectivity for (a) $R(Z)$ (MP48), (b) $R(Z)$ (F98), (c) $R(Z, Z_{DR})$ (BR01), (d) $R(K_{DP}, Z_{DR})$ (BR01), (e) $R(K_{DP})$ (BR11), (f) $R(K_{DP})$ (BR06), (g) $R(K_{DP})$ (B02), (h) $R(A)$ (R14), (i) KBUF reflectivity-derived accumulation from $R(Z)$ (F98), and (j) KBUF DP-QPE algorithm.

Since KBUF was not affected by radome wetting and was also less affected by attenuation than WKR, the spatial distribution of rain accumulation in Figs. 7i and 7j is likely a good representation of the actual accumulation field. Furthermore, the S-band

DP-QPE is more reliable than the S-band $R(Z)$ because of the separation of hail and mixed-phase hydrometeors.

Overall rain accumulation for the $R(Z)$ algorithms with the corrected WKR reflectivity (Figs. 7a,b) are the lowest of all the estimates. The $R(Z)$ rainfall estimates were on average more than 60% lower than KBUF using the NEXRAD dual-polarimetric algorithm. The $R(Z, Z_{DR})$ amounts in Fig. 7c show higher rainfall amounts in general, but the heavier accumulations south of the radar and around the airport are not captured adequately in comparison to Fig. 7j. The $R(K_{DP}, Z_{DR})$ in Fig. 7d shows some improvement. In these two figures (Figs. 7c,d), an artifact from the Z_{DR} attenuation-correction method is present, producing a distorted radial in the accumulation pattern. The $R(K_{DP})$ algorithms (Figs. 7e–g) produce progressively closer accumulations patterns to the S-band DP-QPE accumulation in Fig. 7j. Note that the B02* accumulation is not illustrated here, since its spatial accumulation pattern was very similar to B02 in Fig. 7g. The $R(A)$ in Fig. 7h shows similar amounts to the B02 algorithm (Fig. 7g) and also shows a lot more internal structure in the accumulation field than any of the algorithms from either WKR or KBUF. The C-band rainfall estimates from $R(A)$ have the same spatial resolution as the $R(Z)$ estimates. Overall, the C-band accumulations in Figs. 7g and 7h are the closest visually, in spatial distribution and amounts to the S-band DP-QPE algorithm in Fig. 7j.

There are likely some attenuation effects in the KBUF data, by closely looking at the accumulation based on the F98 $R(Z)$ in Fig. 7i. Although the $R(Z)$ and $R(Z, Z_{DR})$ algorithms produced comparable accumulation for KBUF, $R(Z)$ accumulation in Fig. 7i shows reduced accumulation in areas north and west of the airport (one or two grid blocks from the image center) compared to the same area in Fig. 7j. During the heavy rainfall period from 2100 to 2230 UTC, KBUF measured large radial Φ_{DP} changes, and the corresponding Z were significantly attenuated in these areas at 2200 UTC (Figs. 6g,h). The DP-QPE in Fig. 7j also shows a local maximum rainfall accumulation exceeding 150 mm for a few pixels just northeast of the airport. The corresponding area in the S-band $R(Z)$ estimate only shows about 90 mm of total accumulation. The hydrometeor classification algorithm used in DP-QPE identified hail pixels in this core and used an $R(K_{DP})$ algorithm to estimate the rain in these areas (Berkowitz et al. 2013); $R(Z, Z_{DR})$ was used for pure rain pixels surrounding this core.

All the accumulation images show a relative maximum in the spatial distribution of rainfall total about

5 km east of the airport. The local maximum amounts for the different algorithms were variable, with the lowest rainfall total in the 40–50 mm range for the Z -only algorithms compared to over 150 mm in Fig. 7g (B02), Fig. 7h [$R(A)$], and Fig. 7j (the NEXRAD dual-polarization algorithm).

b. Radar–gauge storm total evaluation

High-temporal-resolution rain gauge data were available at 44 locations, with seven reporting storm total accumulation over 80 mm (Fig. 3). An additional four gave storm total only. The radar rain totals from the various algorithms were determined from the radar pixel (over the gauge) and averaged over 3×3 , 5×5 , and 7×7 range bin by azimuth windows centered at the gauge pixel. There were no significant differences between the window averages (radar pixels), so a 5 range bin by 5 azimuth window average was selected at the gauge locations to produce a spatially averaged rain amount at each scan. Radar-derived rain rates were not time interpolated and were assumed constant over the time between scans. These were summed over the storm duration to produce the radar rainfall total to compare with the gauge totals. Scatterplots of the rainfall totals from the gauges against the 15 (13 for C band, 2 for S band) radar-derived storm totals are shown in Fig. 8 for the algorithms listed in Table 1. To assess the relative performance of the 15 radar-derived storm total estimates relative to the gauge amounts, the following metrics were calculated:

root-mean-square error,

$$\text{RMSE} = \sqrt{\frac{\sum (\text{RT} - \text{GT})^2}{N}};$$

normalized mean bias,

$$\text{NMB} = 100 \left(\frac{\langle \text{RT} \rangle}{\langle \text{GT} \rangle} - 1 \right);$$

normalized standard error,

$$\text{NSE} = \frac{\sqrt{\frac{1}{N} \sum (\text{RT} - \langle \text{RT} \rangle - \text{GT} + \langle \text{GT} \rangle)^2}}{\langle \text{GT} \rangle};$$

and Pearson correlation coefficient,

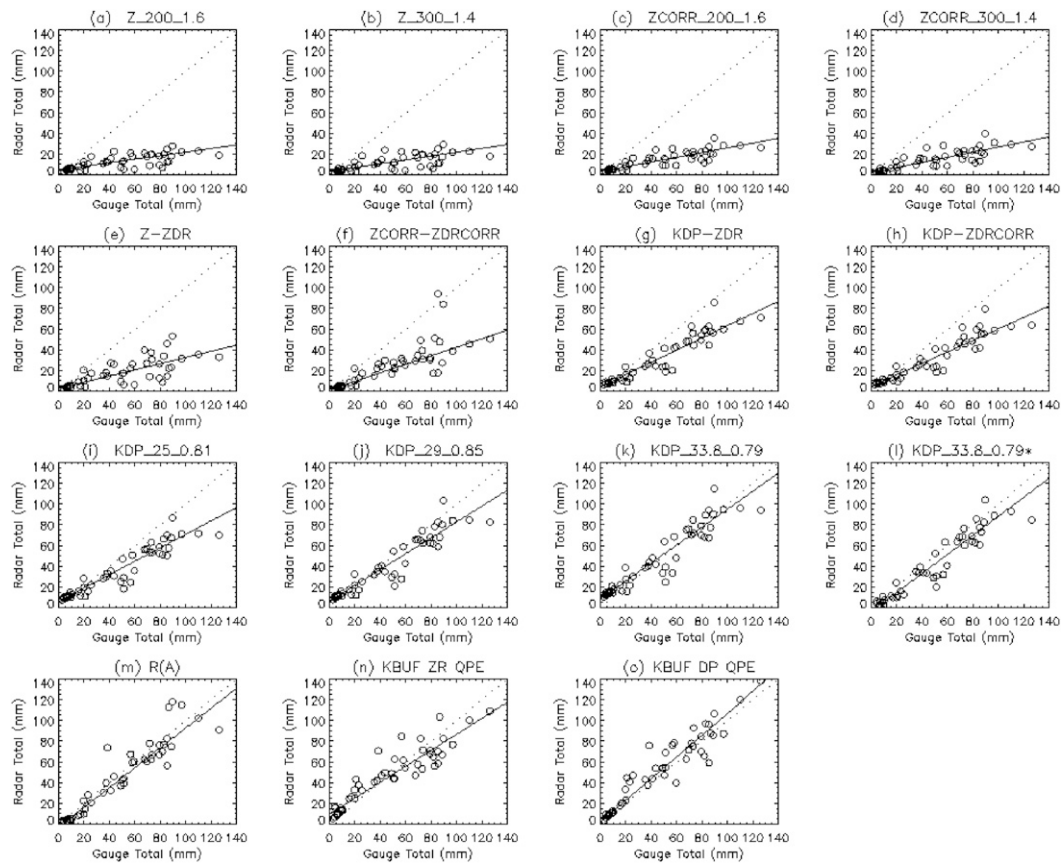


FIG. 8. Scatterplots of radar-derived storm totals against the gauge storm totals for the quantitative precipitation estimators in Table 1.

$$\text{CORR} = \frac{\sum(\text{GT} - \langle \text{GT} \rangle)(\text{RT} - \langle \text{RT} \rangle)}{\sqrt{\sum(\text{GT} - \langle \text{GT} \rangle)^2} \sqrt{\sum(\text{RT} - \langle \text{RT} \rangle)^2}},$$

where GT is the gauge total rainfall amount and RT is the radar-derived total accumulation estimate at the gauge location for N gauges. The quantities in the angle brackets are averages. The results are presented in Table 2.

Least absolute deviation fits of the form $\text{RT} = a\text{GT} + b$ for the 48 gauge–radar pairs were calculated and are represented by the solid lines in the scatterplots. Dotted lines are the one-to-one lines. The following are for the C-band estimates compared to the gauges unless otherwise indicated. The $R(Z)$ and $R(Z, Z_{\text{DR}})$ estimates without and with attenuation correction are shown in Figs. 8a–f. They had best-fit slopes well below 1, and correlation coefficients from Table 2 ranged between 0.71 and 0.85. The RMSE for these estimates ranged between 31 and 50 mm, and NMB ranged from -50% to -75% . The scatter, reflected in the NSE, varied from 46% to 62% for the $R(Z)$ and $R(Z, Z_{\text{DR}})$ estimates.

Although the attenuation correction did improve the uncorrected estimates slightly, it was still not adequate in this situation.

The $R(K_{\text{DP}}, Z_{\text{DR}})$ algorithm in Figs. 8g and 8h (before and after correction of Z_{DR}) performed better than the $R(Z)$ and $R(Z, Z_{\text{DR}})$ estimators, with RMSE of about 20–23 mm and NMB from -35% to -30% . The CORR was excellent at 0.94; however, the NSE was in the 33%–35% range. Although K_{DP} is immune to attenuation, radome wetting, calibration, etc., Z_{DR} seems to be limiting the radar-derived estimates using the $R(K_{\text{DP}}, Z_{\text{DR}})$ algorithm. Interestingly, by using attenuation-corrected Z_{DR} in the $R(K_{\text{DP}}, Z_{\text{DR}})$ algorithm, the RMSE and NSE were slightly larger, 22.8 mm and 35% compared to 20.6 mm and 32%, when the uncorrected Z_{DR} was used. The CORR (0.93) and NMB (-34.5%) were worse compared to 0.94 and -32% with uncorrected Z_{DR} in the algorithm.

The $R(K_{\text{DP}})$ rainfall total estimates for WKR are shown in Figs. 8i–l for the BR11, BR06, B02, and B02* algorithms, compared to the gauge rainfall totals. These algorithms obviously performed much better than the

TABLE 2. Relative performance of each algorithm with respect to the gauge total for the 8 Jul 2013 storm, showing values for RMSE, NMB, NSE, and CORR. The best value in each column is in boldface.

Algorithm	RMSE (mm)	NMB (%)	NSE (%)	CORR
Z_200_1.6	45.0	-74.3	62	0.74
Z_300_1.4	45.4	-75.6	61	0.71
ZCORR_200_1.6	42.2	-70.4	57	0.85
ZCORR_300_1.4	41.9	-70.4	56	0.84
Z-Z _{DR}	38.8	-63.4	54	0.76
ZCORR-Z _{DR} CORR	31.3	-49.4	46	0.80
K _{DP} -Z _{DR}	20.6	-31.1	32	0.94
K _{DP} -Z _{DR} CORR	22.8	-34.5	35	0.93
K _{DP} _25_0.81	18.4	-24.4	31	0.94
K _{DP} _29_0.85	13.4	-11.9	26	0.94
K _{DP} _33.8_0.79	11.5	2.1	25	0.94
K _{DP} _33.8_0.79 ^a	12.9	-16.2	21	0.95
R(A)	12.2	-6.1	25	0.94
BUF_ZR	13.4	0.61	29	0.92
BUF DP-QPE	12.3	11.1	24	0.95

^a Modified B02 algorithm.

$R(Z)$, $R(Z, Z_{DR})$, and $R(K_{DP}, Z_{DR})$ ones at C band (Table 1) and have much better metrics as indicated in Table 2. RMSE was 18 mm for BR11 and was the least (11.5 mm) for the B02 algorithm. The RMSE was only slightly changed by using B02* (12.8 mm). Both BR11 and BR06 were negatively biased, with NMB of -24% and -12%, respectively, as compared to a small positive 2% bias for the B02 algorithm. Inclusion of negative K_{DP} in B02* resulted in a larger negative bias of -16% with respect to the gauges. The scatter reflected in the NSE was the best for B02*, 21% compared to 25% or larger for the remaining algorithms. The correlation coefficients of the $R(K_{DP})$ estimates of storm total with the gauges were all excellent at 0.94, with the highest being 0.95 for B02*. Scatterplot for the $R(A)$ algorithm is shown in Fig. 8m with the RMSE for the $R(A)$ algorithm similar to B02 or B02*, of just over 12 mm and with a negatively biased RMSE of 6%. The NSE was 25% and correlation with the gauges was 0.94.

The scatterplots of KBUF using the $R(Z)$ and DP-QPE of storm totals compared to the gauge totals are shown in Figs. 8n and 8o. The RMSEs were 13 and 12 mm, respectively, with a very small 0.6% bias for the $R(Z)$ amounts and 11% for the DP-QPE amounts. Although the bias was much smaller, the scatter reflected in the NSE was 29% for $R(Z)$ compared to 24% for the dual-polarimetric estimates. The $R(Z)$ correlation was 0.92, smaller than the 0.95 correlation for the S-band DP-QPE. The metrics in Table 2 for the S-band dual-polarimetric storm total estimates are very similar to the C-band B02* algorithm, except for the NMB, which was 11% for the S-band DP-QPE compared

to -16% for the C-band B02* estimates. The difference in sampling heights between the C- and S-band measurements above the gauges was a complicating factor in the interpretation of the statistics and could account for some of the differences.

To illustrate the relative strengths of the methods at high and low rain rates, radar-gauge ratios were calculated for all radar-derived estimates and plotted as a function of the gauge rainfall totals. The ratios are presented in Fig. 9, where an unbiased radar estimate with respect to the gauge would be 1.0. Figures 9a-f are for the WKR estimates based on the forms of rain-rate relationships requiring Z , Z_{DR} , or both. Over the complete range of rain gauge total amounts (3-126 mm), the ratios were much less than 1 and became progressively worse with higher rainfall amounts. The $R(K_{DP}, Z_{DR})$ (Figs. 9g,h) still had ratios much less than 1 for larger amounts, but for low gauge accumulation amounts up to about 15 mm, the radar estimates from this type of estimator were too high because negative values of K_{DP} were chopped off. The $R(K_{DP})$ estimators in Figs. 9i-k also overestimate the lower accumulation because of the use of only positive K_{DP} , but at higher accumulations they are relatively unbiased. Borowska et al. (2011) have utilized both positive and negative K_{DP} to derive relatively unbiased accumulations for light rainfall at X band. However, for this heavy rainfall case, using negative K_{DP} (B02*) resulted in a larger negative mean bias (-16%) for the $R(K_{DP})$ algorithm in Fig. 9l that reduced low accumulation overestimation but also reduced some of the larger accumulation at other gauges. The WKR $R(A)$ ratio in Fig. 9m does not show large overestimation in areas with lower accumulation as most of the $R(K_{DP})$ methods do, but rather shows some underestimation below 20-mm gauge accumulation, similar to B02*. The ratios were smaller over the range of accumulations, and although there was an outlier at the 40-mm gauge amount, the remainder of the estimates had relatively consistent radar-gauge ratios. The KBUF $R(Z)$ and DP-QPE ratios are shown in Figs. 9n and 9o. Two outliers with radar-gauge ratios greater than 3 were present in the KBUF $R(Z)$ estimate. Ignoring these two outliers, the S-band $R(Z)$ ratios ranged from 1 to 2 for a number of gauges with recorded totals less than 50 mm. Also, since the KBUF sampling volume was almost 2 km above the gauges, the VPR effect and sampling volume size (e.g., Fabry et al. 1994; Zawadzki 1975, 1984) complicate the interpretation of the statistics. Similar effects can affect the DP-QPE algorithm, where some of the radar-gauge accumulation ratios were around 2.

c. Selected gauge-radar time series comparison

The 5-min gauge data at 44 locations provided some insight into subhourly accumulation and illustrated the

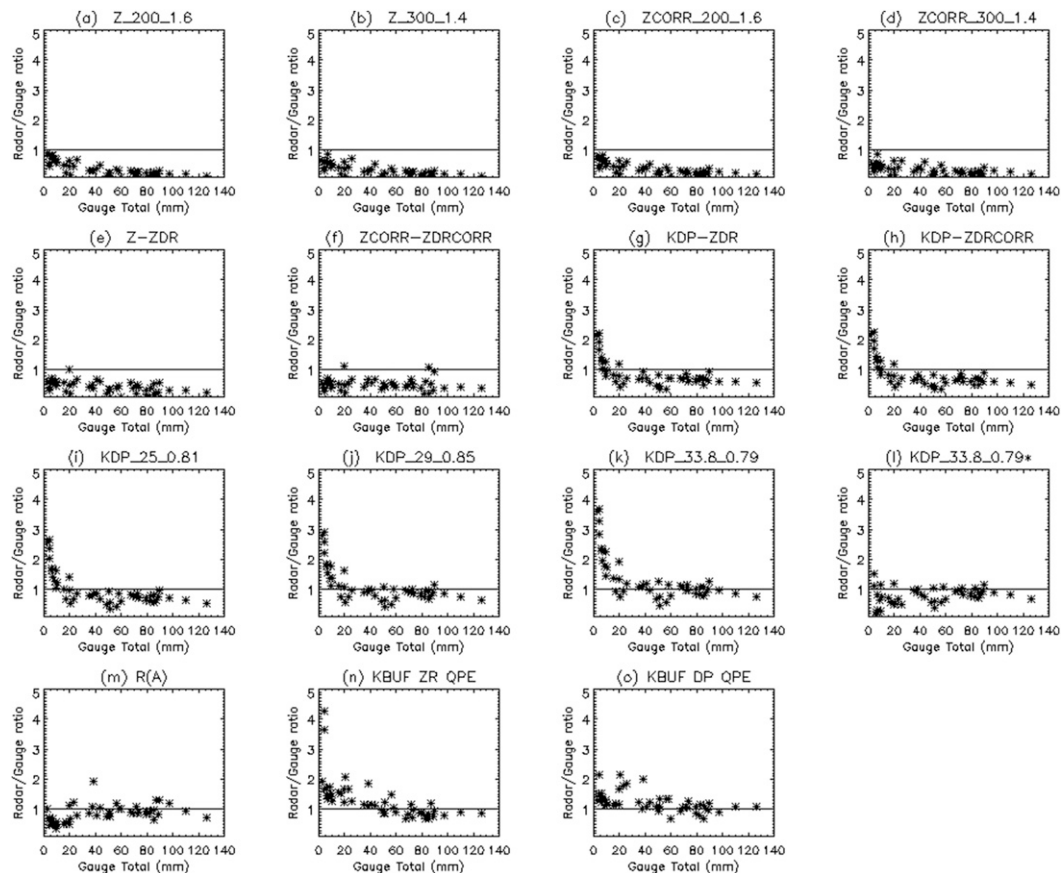


FIG. 9. Ratios of radar–gauge storm total pairs as a function of the gauge storm totals for the quantitative precipitation estimators in Table 1. Each asterisk represents the radar–gauge ratio at each of the 48 gauge locations.

performance of the algorithms in this time frame at various locations in the storm. Figure 10 shows the accumulation time series from the radar-derived estimates and the gauge measurements at two locations. Figure 10a shows the accumulation time series at Mississauga Yard Works station (HY046), which is located 31 km from WKR and is the high-temporal-resolution gauge closest to the maximum recorded storm accumulation at CYYZ. This gauge recorded 109 mm of total rainfall compared to 126 mm at CYYZ. There is an obvious large variation in the final estimates over the accumulation period, ranging from 23 mm, for the $R(Z)$ estimators with uncorrected reflectivity, to 120 mm for the S-band $R(Z, Z_{DR})$ algorithm. The estimates closest to the gauge total (black curve; 109 mm) were from the $R(A)$ algorithm (blue curve; 102 mm). The radar algorithms that followed closely were B02, B02*, the S-band $R(Z)$, and DP-QPE, and all were about ± 10 mm from the gauge amount. Rainfall over the gauge started around 2000 UTC soon after which the WKR $R(Z)$ estimators started deviating from the gauge accumulation because

of radome and path attenuation effects. Initially, both KBUF estimates and all four WKR $R(K_{DP})$ followed the gauge closely until about 2030 UTC, and they subsequently began deviating away from the gauge. The B02 $R(K_{DP})$ matched the gauge again at 2100 UTC but then deviated again, with lower estimates from about 2130 to 0000 UTC 9 July. BR06 and BR11 $R(K_{DP})$ continued to deviate from the gauge, resulting in 84- and 72-mm rain totals. The accumulation curves from B02 and B02* followed each other closely over all times and ended with 96- and 93-mm rainfall accumulation, respectively, about 10% lower than the gauge rainfall total. The $R(A)$ followed both B02 algorithms closely up to 2100 UTC, but then deviated from them and followed the gauge accumulation curve more closely; it resulted in 102 mm of rainfall accumulation, the best radar estimate at this gauge. The KBUF estimates essentially followed the rain gauge accumulation from 2030 to about 2140 UTC, reaching about 60 mm. Both estimates then started deviating from the gauge from 2150 UTC, resulting in KBUF underestimating with $R(Z)$ and

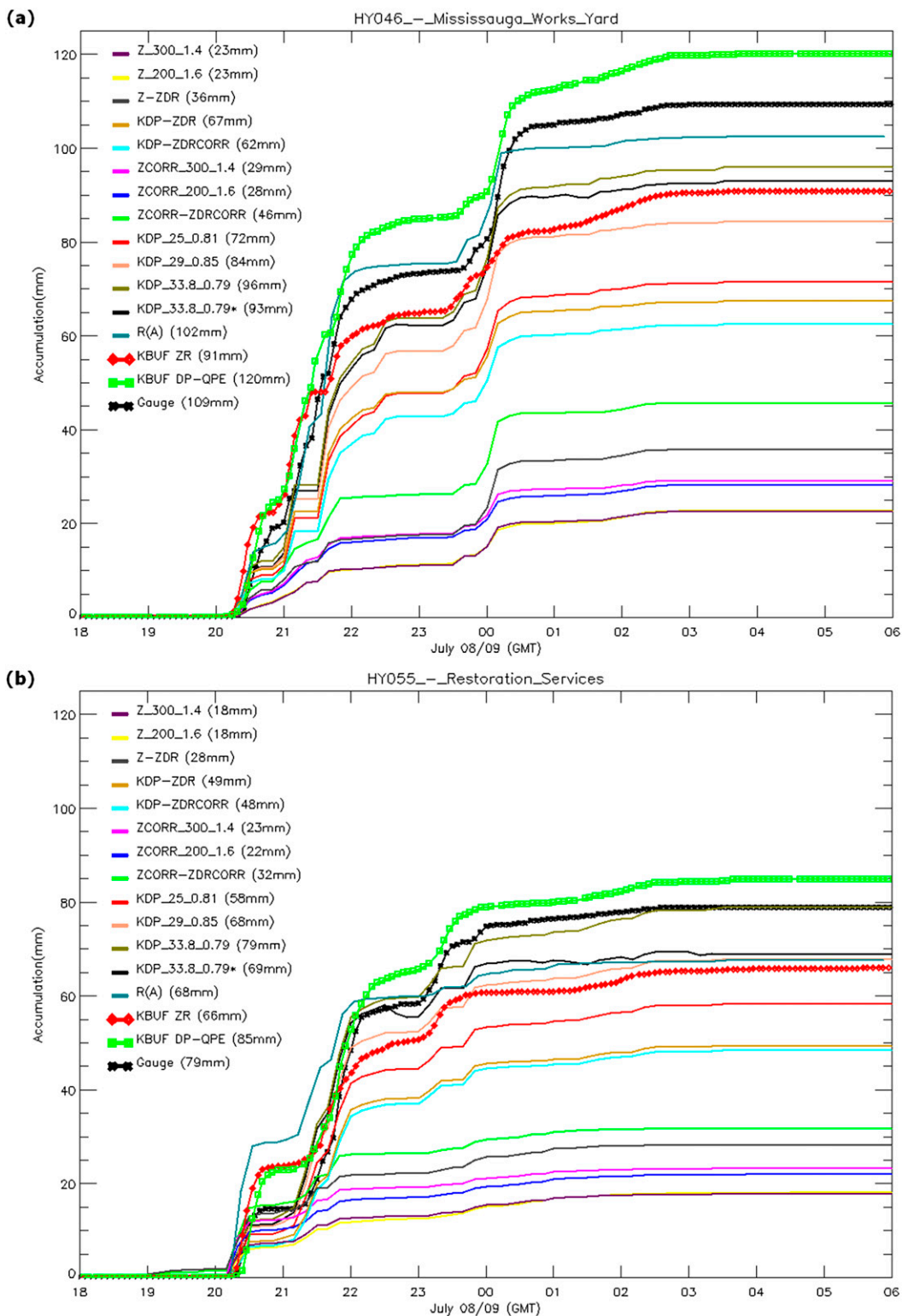


FIG. 10. Rainfall accumulation time series for the various radar rain-rate algorithms in Table 1 and the 5-min resolution gauge data at (a) HY046 and (b) HY055.

overestimating with DP-QPE. Uncertainties from TBRG's rainfall measurements (e.g., Habib et al. 2001; Ciach 2003) can be on the order of 5%–10% and are dependent on the actual rain rate and collection interval. Considering errors in the gauge accumulation, the range of the S-band accumulation estimates (91–120 mm) and the C-band estimates from B02 and B02* (i.e., 96 and 93 mm, respectively) were reasonable.

Figure 10b shows the accumulation time series plot for the Restoration Services (HY055) gauge located 16 km from WKR, which recorded 79 mm of rain total. B02 was in excellent agreement with this amount, whereas B02* was 10 mm lower. The KBUF DP-QPE was just 6 mm higher than the gauge. The $R(Z)$ from KBUF only gave 66 mm by comparison. Note that this gauge is located in the area where KBUF reflectivity was negatively biased because of attenuation, which results in the lower radar-derived amount. During the entire accumulation period, B02 followed the 5-min gauge data very closely with no significant deviation from the gauge accumulation curve. Interestingly, $R(A)$ deviated from the gauge right from the start at 2030 UTC, overestimating rain rates, but later matched the gauge rates and then was underestimating the 10-min accumulations from 2200 UTC onward. B02* initially followed the gauge and the unmodified B02 algorithm closely, but from about 2130 UTC it was more closely correlated with $R(A)$ and resulted in 69 and 68 mm accumulation, respectively. From 2030 to 2130 UTC, the KBUF $R(Z)$ and DP-QPE lines deviated by roughly 10 mm above the gauge. Also from 2200 UTC onward, KBUF $R(Z)$ was lower than the gauge curve for the rest of the accumulation period. The DP-QPE continued to be slightly above the gauge for the remaining time. Examination of the time series for the other gauges may yield further insights; however, it is beyond the scope of this paper.

5. Conclusions

On 8 July 2013, pulse-type storms moved slowly across Toronto, producing flash flooding in certain areas. In the Toronto Pearson International Airport area, storm cells were impeded by the Lake Ontario lake-breeze front and resulted in convective clusters and enhanced heavy rainfall, caused by convergence of the outflow boundaries and the lake-breeze front. The maximum gauge rainfall total was 126 mm at a rain gauge located at CYYZ. WKR and KBUF suggested higher rainfall accumulation a few kilometers to the northeast of the airport.

The major factors affecting radar-derived QPE in this heavy rain event were radome and path attenuation

effects. Ground clutter in the urban environment and contamination from second-trip echoes were handled by applying filtering techniques based on SQI and ρ_{HV} thresholding. Attenuation correction of Z and Z_{DR} were done with a modified ZPHI algorithm. Brightband effects and VPR corrections were not considered important for the C-band radar in this case study, as the radar measurements were a few hundred meters above the surface for all the rain gauge locations. This particular event moved very slowly in comparison to typical summertime convective systems observed in this region. Advection errors and errors in rain gauge rainfall measurement and problems associated with radar–gauge comparisons (e.g., Fabry et al. 1994) have been ignored for this study.

Rainfall estimates from the C-band radar were determined from traditional reflectivity–rain-rate algorithms before and after correction for attenuation. These algorithms yield large negative biases [e.g., -75% for uncorrected $R(Z)$] of rainfall storm accumulation when compared to the 48 gauge amounts. Not surprisingly, $R(Z, Z_{DR})$ also did not perform well because of the heavy radome attenuation occurring for significant periods for this storm. Attenuation correction of Z and Z_{DR} made some but insufficient improvement in mean biases, from -70% for $R(Z)$ methods to -50% for $R(Z, Z_{DR})$ methods. Apart from the significant radome attenuation, improper α and β parameters in the hotspot correction and improper α_0 and β_0 outside the hotspot region could account for insufficient correction of Z and Z_{DR} at certain instances during the storm.

The algorithms based on specific differential phase performed better in comparison with combined reflectivity and differential reflectivity methods. The $R(K_{DP}, Z_{DR})$ algorithm gave about a -30% bias that worsened using attenuation-corrected Z_{DR} (-34%). This was attributed to inconsistencies in the differential reflectivity attenuation correction scheme. Since $R(K_{DP})$ and $R(A)$ are the only algorithms not affected by radome and path attenuation effects, they performed the best in estimating the overall storm accumulations. However, there were significant differences in the storm total accumulation based on the coefficients used in these algorithms; $R(K_{DP})$ algorithms with different parameters were tested in the study. The B02 algorithm (using only positive K_{DP}) gave the least bias, $+2\%$, but large overestimation of rainfall accumulation at lower rates; however, B02* (i.e., including negative K_{DP} in the rain-rate calculations) produced a bias of -16% but removed the overestimation of rainfall at lower rain rates. Furthermore, this latter algorithm produced the least radar–gauge scatter overall but produced negative total accumulation in parts of the storm with lower rain rates.

The specific attenuation algorithm $R(A)$ produces very good results, with a mean overall bias of only -6% together with strong performance on other measures. This algorithm has the advantage of not being as sensitive to DSD variability as the $R(K_{DP})$ algorithms, and it preserved the fine structure details in the accumulation field better than the $R(K_{DP})$ algorithms. Heavy filtering and smoothing of the Φ_{DP} profiles to derive K_{DP} results in a loss of fine details in the $R(K_{DP})$ accumulations. Both $R(A)$ and $R(K_{DP})$ are immune to radar miscalibration and radome wetting impacts.

The NEXRAD S-band radar provided an independent set of rain total estimates, based on S-band reflectivity and the DP-QPE algorithms. Only the $R(K_{DP})$ and $R(A)$ algorithms from the C band produced estimates that were comparable with the S-band estimates. Overall, the $R(K_{DP})$ and $R(A)$ algorithms for the C band gave storm total correlation with the gauges of 0.94, and RMSE of about 12 mm, which were much better than the reflectivity- and differential reflectivity-based algorithms and compared very well with the S-band estimates. This highlights the enormous benefit of dual-polarimetric methods at C band for QPE that can produce results comparable to S band for this complex rainfall case. At low rain rates, $R(K_{DP})$ estimators can be problematic because the possibility of producing unrealistic negative rainfall accumulations or a selective method using K_{DP} in parts of the storm with heavy rainfall and unbiased Z in parts with lighter rainfall could apply. The $R(A)$ algorithm also shows good promise overall.

Future work is required to quantify the losses from the radome wetting and to include that loss in the correction of Z and Z_{DR} . This would help to improve the C-band dual-polarimetric QPE estimates and to resolve some of the problems associated with K_{DP} estimators.

Acknowledgments. The authors would like to acknowledge Joan Klaassen and Rebecca Wagner of Environment Canada for providing Fig. 1, and also the Toronto Regional Conservation Authority and the City of Mississauga for the rain gauge data used in this study. Thanks to Emma Hung for the preparation of Fig. 2 and to Vlado Stojanovic for general radar discussions. We also express our thanks to the reviewers for their comments and suggestions that improved the manuscript.

REFERENCES

- Austin, P. M., 1987: Relation between measured radar reflectivity and surface rainfall. *Mon. Wea. Rev.*, **115**, 1053–1070, doi:10.1175/1520-0493(1987)115<1053:RBMRRR>2.0.CO;2.
- Berkowitz, D. S., J. A. Schultz, S. Vasiloff, K. L. Elmore, C. D. Payne, and J. B. Boettcher, 2013: Status of dual pol QPE in the WSR-88D network. *27th Conf. on Hydrology*, Austin, TX, Amer. Meteor. Soc., 2.2. [Available online at <https://ams.confex.com/ams/93Annual/webprogram/Paper221525.html>.]
- Bolen, S., V. N. Bringi, and V. Chandrasekar, 1998: An optimal area approach to intercomparing polarimetric radar rain rate algorithms with gauge data. *J. Atmos. Oceanic Technol.*, **15**, 605–623, doi:10.1175/1520-0426(1998)015<0605:AOAATI>2.0.CO;2.
- Borowska, L., D. Zrnić, A. Ryzhkov, P. Zhang, and C. Simmer, 2011: Polarimetric estimates of a 1-month accumulation of light rain with a 3-cm wavelength radar. *J. Hydrometeorol.*, **12**, 1024–1039, doi:10.1175/2011JHM1339.1.
- Brandes, E. A., A. V. Ryzhkov, and D. S. Zrnić, 2001: An evaluation of radar rainfall estimates from specific differential phase. *J. Atmos. Oceanic Technol.*, **18**, 363–375, doi:10.1175/1520-0426(2001)018<0363:AEORRE>2.0.CO;2.
- , G. Zhang, and J. Vivekanandan, 2002: Experiments in rainfall estimation with a polarimetric radar in a subtropical environment. *J. Appl. Meteor.*, **41**, 674–685, doi:10.1175/1520-0450(2002)041<0674:EIREWA>2.0.CO;2.
- Bringi, V. N., and V. Chandrasekar, 2001: *Polarimetric Doppler Weather Radar: Principles and Applications*. Cambridge University Press, 636 pp.
- , M. Thurai, K. Nakagawa, G. J. Huang, T. Kobayashi, A. Adachi, H. Hanado, and S. Sekizawa, 2006: Rainfall estimation from C-band polarimetric radar in Okinawa, Japan: Comparisons with 2D-video disdrometer and 400 MHz wind profiler. *J. Meteor. Soc. Japan*, **84**, 705–724, doi:10.2151/jmsj.84.705.
- , M. A. Rico-Ramirez, and M. Thurai, 2011: Rainfall estimation with an operational polarimetric c-band radar in the United Kingdom: Comparison with a gauge network and error analysis. *J. Hydrometeorol.*, **12**, 935–954, doi:10.1175/JHM-D-10-05013.1.
- Čiach, G. J., 2003: Local random errors in tipping-bucket rain gauge measurements. *J. Atmos. Oceanic Technol.*, **20**, 752–759, doi:10.1175/1520-0426(2003)20<752:LREITB>2.0.CO;2.
- Cifelli, R., V. Chandrasekar, S. Lim, P. Kennedy, Y. Wang, and S. Rutledge, 2011: A new dual-polarization radar rainfall algorithm: Application in Colorado precipitation events. *J. Atmos. Oceanic Technol.*, **28**, 352–364, doi:10.1175/2010JTECHA1488.1.
- Cocks, S., D. Berkowitz, R. Murnan, J. Schultz, S. Castleberry, K. Howard, K. Elmore, and S. Vasiloff, 2012: Initial assessment of the dual-polarization quantitative precipitation estimate algorithm's performance for three dual-polarization WSR-88Ds. *28th Conf. on Interactive Information Processing Systems*, New Orleans, LA, Amer. Meteor. Soc., 7B.2. [Available online at <https://ams.confex.com/ams/92Annual/webprogram/Paper203568.html>.]
- Cunha, L. K., J. A. Smith, M. L. Baeck, and W. F. Krajewski, 2013: An early performance evaluation of the NEXRAD dual-polarization radar rainfall estimates for urban flood applications. *Wea. Forecasting*, **28**, 1478–1497, doi:10.1175/WAF-D-13-00046.1.
- Diederich, M., S. Troemel, A. Ryzhkov, P. Zhang, and C. Simmer, 2015a: Use of specific attenuation for rainfall measurements at X-band radar wavelengths. Part I: Radar calibration and partial beam blockage estimation. *J. Hydrometeorol.*, **16**, 487–502, doi:10.1175/JHM-D-14-0066.1.
- , —, —, —, and —, 2015b: Use of specific attenuation for rainfall measurements at X-band radar wavelengths. Part

- II: Rainfall estimates and comparison with rain gauges. *J. Hydrometeorol.*, **16**, 503–516, doi:10.1175/JHM-D-14-0067.1.
- Fabry, F., A. Bellon, M. R. Duncan, and G. L. Austin, 1994: High-resolution rainfall measurements by radar for very small basins: The sampling problem reexamined. *J. Hydrol.*, **161**, 415–428, doi:10.1016/0022-1694(94)90138-4.
- Fulton, R. A., J. P. Breidenbach, D.-J. Seo, D. A. Miller, and T. O'Bannon, 1998: The WSR-88D rainfall algorithm. *Wea. Forecasting*, **13**, 377–395, doi:10.1175/1520-0434(1998)013<0377:TWRA>2.0.CO;2.
- Giangrande, S. E., and A. V. Ryzhkov, 2008: Estimation of rainfall based on the results of polarimetric echo classification. *J. Appl. Meteorol.*, **47**, 2445–2462, doi:10.1175/2008JAMC1753.1.
- , S. Collis, A. K. Theisen, and A. Tokay, 2014: Precipitation estimation from the ARM distributed radar network during the MC3E campaign. *J. Appl. Meteor. Climatol.*, **53**, 2130–2147, doi:10.1175/JAMC-D-13-0321.1.
- Gorgucci, E., G. Scarchilli, V. Chandrasekar, and V. N. Bringi, 2001: Rainfall estimation from polarimetric radar measurements: Composite algorithms immune to variability in raindrop shape–size relation. *J. Atmos. Oceanic Technol.*, **18**, 1773–1786, doi:10.1175/1520-0426(2001)018<1773:REFPRM>2.0.CO;2.
- Gourley, J. J., P. Tabary, and J. Parent du Chatelet, 2007: A fuzzy logic algorithm for the separation of precipitating from non-precipitating echoes using polarimetric radar observations. *J. Atmos. Oceanic Technol.*, **24**, 1439–1451, doi:10.1175/JTECH2035.1.
- Gu, J.-Y., A. Ryzhkov, P. Zhang, P. Neilley, M. Knight, B. Wolf, and D.-I. Lee, 2011: Polarimetric attenuation correction in heavy rain at C band. *J. Appl. Meteor. Climatol.*, **50**, 39–58, doi:10.1175/2010JAMC2258.1.
- Habib, E., W. F. Krajewski, and A. Kruger, 2001: Sampling errors of tipping-bucket rain gauge measurements. *J. Hydrol. Eng.*, **6**, 159–166, doi:10.1061/(ASCE)1084-0699(2001)6:2(159).
- Illingworth, A. J., and R. J. Thompson, 2005: The estimation of moderate rain rates with operational polarisation radar. *32nd Int. Conf. on Radar Meteorology*, Albuquerque, NM, Amer. Meteor. Soc., P9R.1. [Available online at <https://ams.confex.com/ams/pdfpapers/96204.pdf>.]
- Joss, J., and A. Waldvogel, 1990: Precipitation measurement and hydrology. *Radar in Meteorology*, D. Atlas, Ed., Amer. Meteor. Soc., 577–606.
- Krajewski, W. F., G. Villarini, and J. A. Smith, 2010: Radar-rainfall uncertainties. *Bull. Amer. Meteor. Soc.*, **91**, 87–94, doi:10.1175/2009BAMS2747.1.
- Liu, H., and V. Chandrasekar, 2000: Classification of hydrometeors based on polarimetric radar measurements: Development of fuzzy logic and neuro-fuzzy systems, and in situ verification. *J. Atmos. Oceanic Technol.*, **17**, 140–164, doi:10.1175/1520-0426(2000)017<0140:COHBOP>2.0.CO;2.
- Marshall, J. S., and W. M. Palmer, 1948: The distribution of raindrops with size. *J. Meteorol.*, **5**, 165–166, doi:10.1175/1520-0469(1948)005<0165:TDORWS>2.0.CO;2.
- Park, H. S., A. V. Ryzhkov, D. S. Zrnić, and K. E. Kim, 2009: The hydrometeor classification algorithm for the polarimetric WSR-88D: Description and application to an MCS. *Wea. Forecasting*, **24**, 730–748, doi:10.1175/2008WAF2222205.1.
- Richards, W., and C. L. Crozier, 1983: Precipitation measurement with a C-band radar in southern Ontario. *Atmos.–Ocean*, **21**, 125–137, doi:10.1080/07055900.1983.9649160.
- Ryzhkov, A. V., and D. S. Zrnić, 1996: Assessment of rainfall measurement that uses specific differential phase. *J. Appl. Meteorol.*, **35**, 2080–2090, doi:10.1175/1520-0450(1996)035<2080:AORMTU>2.0.CO;2.
- , and —, 1998a: Discrimination between rain and snow with a polarimetric radar. *J. Appl. Meteorol.*, **37**, 1228–1240, doi:10.1175/1520-0450(1998)037<1228:DBRASW>2.0.CO;2.
- , and —, 1998b: Beamwidth effects on the differential phase measurements of rain. *J. Atmos. Oceanic Technol.*, **15**, 624–634, doi:10.1175/1520-0426(1998)015<0624:BEOTDP>2.0.CO;2.
- , S. Giangrande, and T. Schuur, 2005a: Rainfall estimation with a polarimetric prototype of the WSR-88D radar. *J. Appl. Meteorol.*, **44**, 502–515, doi:10.1175/JAM2213.1.
- , T. J. Schuur, D. W. Burgess, P. L. Heinselman, S. E. Giangrande, and D. S. Zrnić, 2005b: The Joint Polarization Experiment: Polarimetric rainfall measurements and hydrometeor classification. *Bull. Amer. Meteor. Soc.*, **86**, 809–824, doi:10.1175/BAMS-86-6-809.
- , D. Hudak, and J. Scott, 2006: A new polarimetric scheme for attenuation correction at C band. *Fourth European Conf. on Radar in Meteorology and Hydrology*, Barcelona, Spain, ERAD, 29–32. [Available online at www.crahi.upc.edu/ERAD2006/proceedingsMask/00008.pdf.]
- , P. Zhang, D. Hudak, J. L. Alford, M. Knight, and J. W. Conway, 2007: Validation of polarimetric methods for attenuation correction at C band. *33rd Conf. on Radar Meteorology*, Cairns, Australia, Amer. Meteor. Soc., P11B.12. [Available online at <https://ams.confex.com/ams/pdfpapers/123122.pdf>.]
- , M. Diederich, P. Zhang, and C. Simmer, 2014: Potential utilization of specific attenuation for rainfall estimation, mitigation of partial beam blockage, and radar networking. *J. Atmos. Oceanic Technol.*, **31**, 599–619, doi:10.1175/JTECH-D-13-00038.1.
- Scarchilli, G., E. Gorgucci, V. Chandrasekar, and T. A. Seliga, 1993: Rainfall estimation using polarimetric techniques at C-band frequencies. *J. Appl. Meteorol.*, **32**, 1150–1160, doi:10.1175/1520-0450(1993)032<1150:REUPTA>2.0.CO;2.
- Sills, D. M. L., J. R. Brook, I. Levy, P. A. Makar, J. Zhang, and P. A. Taylor, 2011: Lake breezes in the southern Great Lakes region and their influence during BAQS-Met 2007. *Atmos. Chem. Phys.*, **11**, 7955–7973, doi:10.5194/acp-11-7955-2011.
- Tabary, P., 2007: The new French operational radar rainfall product. Part I: Methodology. *Wea. Forecasting*, **22**, 393–408, doi:10.1175/WAF1004.1.
- , A.-A. Boumahmoud, H. Andrieu, R. J. Thompson, A. J. Illingworth, E. LeBouar, and J. Testud, 2011: Evaluation of two “integrated” polarimetric quantitative precipitation estimation (QPE) algorithms at C-band. *J. Hydrol.*, **405**, 248–260, doi:10.1016/j.jhydrol.2011.05.021.
- Testud, J., E. Le Bouar, E. Obligis, and M. Ali-Mehenni, 2000: The rain profiling algorithm applied to polarimetric weather radar. *J. Atmos. Oceanic Technol.*, **17**, 332–356, doi:10.1175/1520-0426(2000)017<0332:TRPAAT>2.0.CO;2.
- Wang, Y., P. Zhang, A. Ryzhkov, J. Zhang, and P.-L. Chang, 2014: Utilization of specific attenuation for tropical rainfall estimation in complex terrain. *J. Hydrometeorol.*, **15**, 2250–2266, doi:10.1175/JHM-D-14-0003.1.
- Zawadzki, I., 1975: On radar–raingage comparison. *J. Appl. Meteorol.*, **14**, 1430–1436, doi:10.1175/1520-0450(1975)014<1430:ORRC>2.0.CO;2.
- , 1984: Factors affecting the precision of radar measurements of rain. Preprints, *22nd Conf. on Radar Meteorology*, Zurich, Switzerland, Amer. Meteor. Soc., 251–256.